International Journal of Material Forming (2026) 19:43
https://doi.org/10.1007/s12289-026-01999-8

RESEARCH

Development and experimental validation of a path-dependent spin forming finite element model

Elizabeth Urig[1,2] · Leonid V. Zhigilei[1]

Received: 1 December 2025 / Accepted: 2 March 2026

Abstract

Spin forming is an advanced manufacturing process widely used in the aerospace and defense sectors to produce lightweight, high-strength cylindrical components with tight dimensional tolerances. This study explores the applicability of the path-dependent Mechanical Threshold Stress (MTS) constitutive model by simulating the evolution of geometry, machining forces, and plastic deformation during the spin forming of a 10-mm thick 6061-O aluminum cylinder. While numerical modeling of spin forming has advanced substantially over the past decade, systematic verification and experimental validation of material models remain limited, particularly in predicting through-thickness process evolution. The MTS model, incorporating a Voce hardening rule, is employed for its ability to represent cyclic loading, rapidly varying temperature fields, and strain rates characteristic of spin forming. Numerical convergence analysis indicates discretization uncertainties between 0.3% and 9.2% for key quantities of interest. Experimental validation demonstrates that the MTS model, when implemented with a verified mesh, accurately reproduces both elastic and plastic behavior of 6061-O aluminum, predicting peak roller loads within 11–18% of measurements, geometric tolerances within 3%, and plastic strain distributions within 10% of experimental values. Collectively, these results establish a validated computational framework for predictive spin-forming simulations with quantified confidence, providing a foundation for extension to other alloys, geometries, and forming conditions.

Keywords Spin forming · Metallic manufacturing · Mechanical threshold stress model · Finite element modeling

Introduction

Computational modeling of spin and flow forming has been an active research area for several decades. Despite steady advances in computational methodology, accurately capturing the complex stress states and incremental plastic deformation inherent to these processes remains challenging. As a result, the predictive capability of finite element models for process optimization is still limited [1]. Existing studies generally fall into three categories: (i) improving constitutive laws to better describe the material response to mechanical loading [2–8], (ii) employing simplifying assumptions to enhance computational efficiency [9–13], and (iii) modeling limited time intervals of the forming process to investigate steady-state behavior [14–17].

The loading conditions in spin forming are highly triaxial and non-monotonic, necessitating elasto-plastic material models that incorporate temperature and strain-rate dependence to capture both plastic deformation and residual stresses [2–4]. Beyond such dependences, constitutive models accounting for deformation history and loading sequence have also been considered [5]. For example, Roula et al. evaluated the applicability of common path-independent constitutive laws (power-law, Hollomon, Johnson–Cook) for modeling aluminum alloy forming and demonstrated the need for more advanced descriptions, such as the Chaboche model with cyclic loading and kinematic hardening [6]. The need for path-dependent descriptions has also been highlighted by Perić et al. [7] and Biba et al. [8], who emphasized the role of elastic–viscoplastic models in simulations of flow forming.

Once a constitutive model is selected, the discretization strategy and simplifying assumptions become critical.

✉ Elizabeth Urig
edu7fe@virginia.edu

1 Department of Materials Science and Engineering, University of Virginia, Charlottesville, VA 22904-4745, USA

2 Analytical Mechanics Associates, Hampton, VA 23666, USA

Published online: 17 April 2026

Many spin forming studies have employed shell elements to efficiently model thin-walled processes [9–13]. These approaches have successfully captured global phenomena such as damage accumulation, bending-under-tension spin forming pathways, and force response for wall thicknesses below 4 mm. In particular, the thin-walled processes benefit from the more mature fields of sheet metal forming and incremental forming, such as single- and double-point incremental forming (SPIF and DPIF). The incremental forming processes have significant overlap with thin-walled spin forming and provide translatable insights into ductile damage prediction, mixed isotropic–kinematic hardening with anisotropic yield behavior, and global formability metrics [18–20]. However, shell element assumptions limit the ability to resolve through-thickness behavior, restricting their applicability to thin-walled parts.

For thicker preforms, research on cyclic forming remains less mature and has primarily focused on flow forming against rigid mandrels [14–17]. In these cases, wall thickness is intentionally reduced, and the material response approaches a steady-state in each mandrel revolution due to the rigid boundary condition imposed by the mandrel. While analysis of steady-state processes provides insight into local roller–material interactions, the degree of localization required for model convergence limits its ability to capture the transient, global effects of multi-pass rotary forming.

Despite advances in modeling thin-walled spin forming and steady-state flow forming, a critical gap remains: a validated computational framework for predicting the through-thickness mechanical response of thick (>4 mm) spin-formed plates subjected to transient, multi-pass deformation is still lacking. This gap motivates the present work, which develops a fully three-dimensional (3D) solid-element framework capable of resolving stress evolution and transient global effects across the entire free-space spin forming process.

The path-dependent Mechanical Threshold Stress (MTS) constitutive model [5, 21, 22] is implemented within the finite element framework to capture material hardening and deformation history effects under the large plastic strains, rapidly varying strain rates, and temperature fields characteristic of spin forming. The predictive capability of the model is assessed through systematic numerical verification and multi-modal experimental validation, including comparisons of roller forces, deformation geometry, temperature evolution, and plastic strain distributions.

Computational and experimental methodology

The benchmark simulation is based on an Al 6061-O aluminum spin forming experiment commonly performed on the VUD-600 at NASA Langley. The workpiece consists of an annealed Al 6061-O disk (diameter of 220 mm and thickness of 10 mm), clamped between a mandrel and a tailstock and rotated at 400 rpm. Localized axisymmetric deformation is introduced by two rollers over five vertical passes of the rollers. Figure 1 illustrates the experimental tooling setup and the corresponding finite element model.

Previous experimental studies have examined the influence of alloy selection, toolpath geometry, and forming speed on process success, microstructure, and mechanical response of spin-formed parts [23, 24]. These investigations identified two regions requiring further analysis with finite element modeling: (i) the clamped region, where the plate bends orthogonally to form the cup shape, and (ii) the localized mechanical work and strain field beneath the roller. In the schematic of the spin forming part cross-section shown in Fig. 2, these regions are outlined by red rectangles.

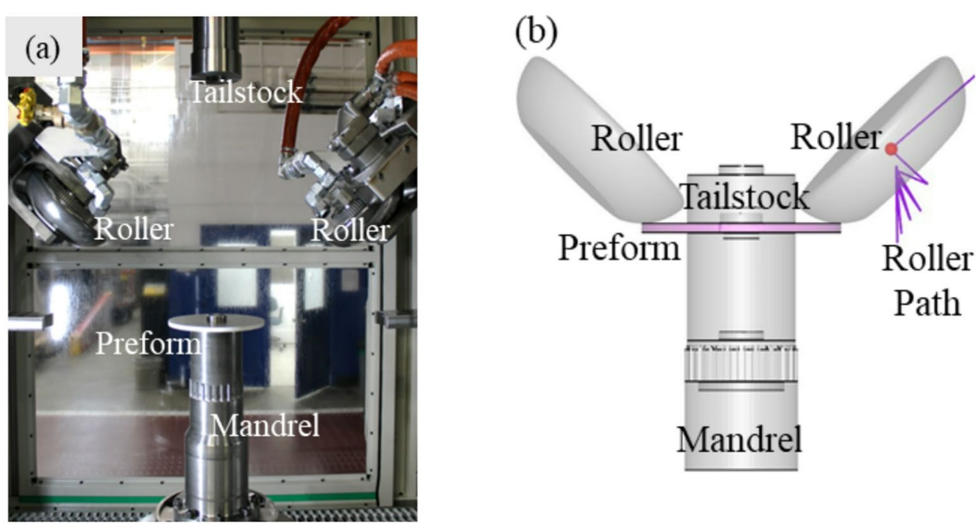

Fig. 1 Experimental (**a**) and computational (**b**) spin forming tooling, showing the mandrel, tailstock, preform, and rollers. The preform undergoes deformation as the rollers impart localized mechanical work

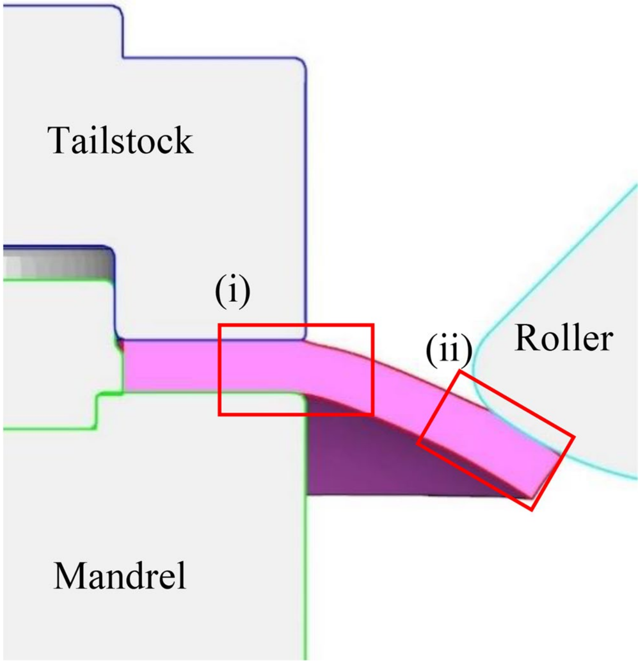

Fig. 2 Cross-section of the benchmark spin-formed part during the first pass, highlighting the regions of interest that are in the focus of finite element modeling: (i) the clamped region and (ii) the localized roller contact, indicated by red rectangles

Computational methodology

The finite element model was developed in DEFORM®, a continuum-level deformation modeling software suitable for simulation of metal forming processes. Simulations were performed with an implicit Newton-Raphson scheme using an Augmented Eulerian–Lagrangian (ALE) solver and a time step of 0.5 ms. Temperature-dependent elastic and plastic contributions were included in the constitutive response to capture springback and residual stresses. The preform was discretized using ~220,000 first-order tetrahedral elements with an average edge length of 1.55 mm, resulting in approximately six elements through the 10 mm thickness of the preform. This edge length was selected empirically to balance computational speed and stress convergence accuracy, while insuring a plane-stress condition on the free surfaces [25]. A locally refined mesh region spanning a 15° wedge of the geometry employed elements with an average edge length of 0.6 mm, enabling accurate resolution of local stress and strain conditions while maintaining reasonable computational efficiency.

Adaptive remeshing was implemented through the software's internal meshing algorithm, triggered when relative contact interference reaches 30% of the local element edge length, or when individual elements experienced 50% deformation (stretch or compression) relative to their initial size. Under these criteria, remeshing occurred during approximately 0.3% of the simulated time steps.

The mandrel, tailstock, and both forming rollers were modeled as rigid bodies. Thermal interactions between all components assumed contact between aluminum 6061-O and hardened tool steel, represented through an effective conductive heat transfer coefficient to account for pressurized interfaces. The tailstock-preform interface was assigned a sticking contact condition (no relative motion), while all other interfaces employed a constant shear friction model. Heat generation from both plastic deformation and frictional contact was included in the coupled thermal-mechanical analysis.

With this configuration, on a local desktop computer (Dell Precision 7910 Workstation with 16-core Intel Xeon processor and 64 GB RAM) each time step required ~ 80 computational seconds, and the full spin forming simulation took approximately 4.5 weeks.

Constitutive model

The Mechanical Threshold Stress (MTS) model was selected as the governing constitutive framework for Al 6061-O [26]. MTS was chosen over more traditional models, such as Hollomon and Johnson–Cook, because it explicitly accounts for inherent microstructural path dependence [5, 21]. This path dependence is tracked through an internal state variable ($\widehat{\sigma}$), which serves as an aggregate macroscopic descriptor of intrinsic material strength arising from the evolution of dislocation density as a function of temperature, strain rate, and strain history. Although kinematic hardening formulations provide directional dependence and anisotropic capabilities, the MTS framework captures viscoplastic material behavior under complex loading conditions through the evolution of the total stress magnitude rather than stress directionality. This feature is particularly important for spin forming, where repeated loading–unloading cycles and high redundant strains are prevalent. In such regimes, path-independent models tend to overestimate material strength, leading to inaccurate predictions of forming forces and deformation.

In MTS, the flow stress is expressed as the sum of an athermal contribution and a thermally activated component [5, 21]. Plastic deformation is described through a visco-plastic formulation that incorporates Voce-type saturation hardening, as well as strain rate and temperature dependences. The governing expression for the flow stress,

$$\sigma = \sigma_a + \frac{\mu(T)}{\mu_0} s_\epsilon\left(\dot{\varepsilon}, T\right) \widehat{\sigma}(\varepsilon, \dot{\varepsilon}, T) \tag{1}$$

relates the flow stress σ to the athermal yield stress σ_a, the temperature-dependent shear modulus $\mu(T)$ normalized by its 0 K reference value of μ_0, the state function $s_\varepsilon(\dot{\varepsilon}, T)$ describing the dependence of the activation energy for dislocation motion on the instantaneous strain rate $\dot{\varepsilon}$ and absolute temperature T, and the mechanical threshold stress $\widehat{\sigma}(\varepsilon, \dot{\varepsilon}, T)$ defined by the strain ε, strain rate, and temperature.

The temperature dependence of the shear modulus $\mu(T)$ is described by an empirical equation [27] with two fitting parameters, D_0 and T_0, determined for the material of interest,

$$\mu(T) = \mu_0 - \frac{D_0}{\exp\frac{T_0}{T} - 1}\,. \tag{2}$$

The state function $s_\varepsilon\left(\dot{\varepsilon}, T\right)$ bears similarity to the mechanical equation of state and quantifies the energy needed for a dislocation to pass a microstructural obstacle. It can be described by the following equation [21],

$$s_\varepsilon\left(\dot{\varepsilon}, T\right) = \left\{1 - \left[\frac{kT}{g_0 \mu(T) b^3} ln\left(\frac{\dot{\varepsilon}_0}{\dot{\varepsilon}}\right)\right]^{\frac{1}{q}}\right\}^{\frac{1}{p}}, \tag{3}$$

where k is Boltzmann constant, p and q are material-specific model parameters, g_0 is the normalized activation energy, b is the magnitude of Burgers vector, $\dot{\varepsilon}_0$ is a reference strain rate [21, 28, 29].

The mechanical threshold stress $\widehat{\sigma}$, required for evaluation of the flow stress in Eq. 1, evolves according to a Voce-type hardening law. The incremental change of the threshold stress with strain,

$$\frac{d\widehat{\sigma}}{d\epsilon} = \Theta_{II}\left(1 - \frac{\widehat{\sigma}}{\widehat{\sigma_s}\left(\dot{\varepsilon}, T\right)}\right), \tag{4}$$

captures stage II work hardening, where Θ_{II} is a material dependent empirical hardening rate coefficient and $\widehat{\sigma_s}\left(\dot{\varepsilon}, T\right)$ is the temperature and strain rate dependent saturation stress. The latter is determined by the following equation [30],

$$ln\widehat{\sigma_s}\left(\dot{\epsilon}, T\right) = ln\widehat{\sigma_{s0}} + \frac{kT}{\mu(T) b^3 g_0} ln\left(\frac{\dot{\varepsilon}}{\dot{\varepsilon}_0}\right), \tag{5}$$

where $\widehat{\sigma_{s0}}$ is the saturation stress at 0 K.

For implementation into the numerical flow stress finite element model, the mechanical threshold stress is explicitly determined as a product of the derivative with respect to strain given by Eq. 4, the instantaneous strain rate, and the time increment,

$$\widehat{\sigma} = \frac{d\widehat{\sigma}}{d\varepsilon}\dot{\varepsilon}dt\,. \tag{6}$$

The material-specific properties are obtained from literature and an Al 6061-O database of ten stress-strain curves measured at varying strain rates and temperatures [26, 31]. All material constants and data sources are provided in Table 1.

Thermal effects

Heat generation in the preform is assumed to arise from mechanical deformation work and frictional effects. The governing equation for heat generation due to mechanical deformation is:

$$\dot{R_{gen}} = \eta \boldsymbol{\sigma} \dot{\boldsymbol{\varepsilon}} \tag{7}$$

where $\dot{R_{gen}}$ is the heat generation rate, η is the mechanical work to heat conversion efficiency (taken as 0.9, typical for metal forming processes), $\boldsymbol{\sigma}$ is the stress tensor, and $\dot{\boldsymbol{\varepsilon}}$ is the strain rate tensor [33, 34].

Generated heat is dissipated through conduction within the aluminum preform, convection to the environment (still air at T_{env} = 20 °C is assumed), and contact conductance to the tool steel mandrel, rollers, and tailstock, represented by an overall heat transfer coefficient h_c. The value of h_c is chosen to be within a broad range of values reported for aluminum alloys under pressure (114–34600 $Wm^{-2}K^{-1}$) [35]. In addition to influencing the constitutive model, the variation of temperature also produces thermal strains incorporated into the elastic response. As a

Table 1 Parameters of the MTS constitutive model for Al 6061-O, obtained by analytical curve fitting of stress–strain data and used for numerical iteration of flow stress values across different strain rates and temperatures

Parameter	Value	Reference
μ_0	28.82 GPa	[31]
D_0	3.44 GPa	[21]
T_0	215 K	[21]
σ_a	5.682 MPa	[31]
$\frac{\Theta_{II}}{\mu_0}$	0.23	[26, 32]
b	$2.86 \cdot 10^{-10} m$	[21]
$\dot{\varepsilon}_0$	$10^7 s^{-1}$	[21]
g_0	0.0947	[26]
$\frac{\widehat{\sigma_{s0}}}{\mu_0}$	0.0136	[26]
p	60.5	[29]
q	1.5	[29]

simplifying assumption, constant values of all thermal properties, including the thermal conductivity k, heat capacity c, and coefficient of thermal expansion α, are assumed in the simulation and are listed in Table 2.

Additionally, shear friction at the contacting interfaces between the preform and the mandrel, as well as between the preform to the two forming rollers, is modeled using a constant shear friction criterion with a friction factor of $m = 0.12$, consistent with values commonly adopted for cold-work bulk forming operations [28]. The frictional shear stress is defined as

$$F_s = m\tau_y \tag{8}$$

where F_s is the frictional stress, m is the friction factor, and τ_y is the shear yield stress. The corresponding rate of heat generation due to frictional sliding is given by

$$\dot{R_\mu} = F_s v_{rel} \tag{9}$$

where $\dot{R}_\mu$ is the frictional heat generation rate and v_{rel} is the relative velocity of the contacting surfaces.

Convergence studies and verification

Time step convergence is supported by an internal substepping feature in the solver. As velocity and force residuals are evaluated, the time step is automatically reduced to ensure convergence. This allows larger time steps when deformation is moderate, while retaining precision during periods of high deformation. Individual time steps are considered converged when the relative velocity norm (the aggregate nodal velocity error relative to the previous estimation) is below 0.05, and the relative force norm (defined analogously) is below 0.1.

A mesh refinement study is conducted using the convergence criteria index following Roache [38]. A model is considered convergent when the result of interest varies monotonically and exhibits decreasing changes with proportionally finer mesh sizes. In a mesh convergence study performed on successively finer meshes, with solutions f_1 (coarse mesh), f_2 (intermediate mesh), and f_3 (fine mesh), the Roache constraints can be written as

$$(f_2 - f_1)(f_3 - f_2) > 0 \tag{10}$$

and

$$|f_2 - f_1| > |f_3 - f_2|. \tag{11}$$

Richardson extrapolation and calculation of the grid convergence index (GCI) are used to determine the rate of convergence and mesh accuracy [39, 40]. The refinement ratio r is taken as $r = L_2/L_3$, a constant representing the ratio of element lengths (L) of the mesh reduction, typically between 1.2 and 2 [39]. The order of convergence n is then calculated as

$$n = ln\left(\frac{f_3 - f_2}{f_2 - f_1}\right)/ln(r) \ , \tag{12}$$

while the theoretical asymptotic value for the result of interest in the limit of vanishing mesh size ($h \to 0$) is evaluated as

$$f_{h=0} \cong \frac{f_2 + (f_1 - f_2)r^n}{r^n - 1}. \tag{13}$$

Finally, the GCI is calculated as

$$GCI = F_s\frac{|err|}{r^n - 1} \ , \tag{14}$$

where F_s is the factor of safety needed for the results (taken to be 1), and the relative error *err* is defined as $err = (f_3 - f_2)/f_2$. Generally, the model is considered robust and converged when the error is below 1% [28].

Table 2 Thermal properties of the Al 6061-O preform used for modeling of the heat generation and dissipation, assumed to be constant over the temperature range realized in the simulations

Parameter	Value	Reference
η	0.9	[33, 34]
α	$22 \cdot 10^{-6}\ K^{-1}$	[28]
k	$180.175\ Wm^{-1}K^{-1}$	[36]
c	$2.43 \cdot 10^{6}\ Jm^{-3}K^{-1}$	[37]
h_c	$5\ kWm^{-2}K^{-1}$	[35]
T_{env}	20 °C	---

Experimental methodology

Three independent experimental measurements are used to validate the finite element model: (i) forming loads on the rollers, (ii) geometric profiles obtained through 3D light scanning, and (iii) plastic strain distribution obtained from hardness mapping. By combining validation across these distinct and independently measured datasets, confidence in both the accuracy of the finite element model and the suitability of the constitutive law is established.

Forming loads are acquired in situ using the VUD-600 data acquisition system, which records positioning, pressures, and feedback currents from the forming equipment at a sampling rate of 125 Hz. For validation purposes, forming loads on the two rollers are obtained from readings of differential hydraulic pressure in the horizontal and vertical directions [23].

To capture the transient geometry of the spin-formed part, the forming process was interrupted after each pass. The intermediate geometries were measured non-destructively using a Creaform MetraSCAN 750 Elite structured light scanner, capable of resolving 3D surfaces with a precision of up to 0.05 mm. To relate these intermediate formed geometries to the computational predictions, the corresponding stress states and shapes predicted in the coupled thermo-mechanical simulation at the matching time steps were used as initial conditions in separate purely elastic simulations. This approach accounts for elastic spring-back occurring when the part is removed from the forming machine mid-deformation.

The temperature evolution during the spin forming process is not directly measured in the experiments. However, a semi-quantitative comparison with computational predictions on the deformation-induced heating can still be established through analysis of video recordings. The onset of visible water vapor provides an indicator of when and where the preform temperature exceeds 100 °C, enabling comparison with the simulated evolution of the temperature distribution.

Finally, plastic strain distributions were obtained through hardness indentation mapping. Two samples from the first spin forming pass were sectioned and tested using Vickers micro-indentation following ASTM E384, with a 100-gf load applied on a Struers indenter system [41]. Hardness–strain correlations were established using the methodology of Haghshenas et al. [42], which relates measured hardness values to accumulated plastic strain. The calibration equations are expressed as:

$$H\left(\varepsilon_p\right) = A\left(\varepsilon_p + \varepsilon_{ind}\right)^B \ , \tag{15}$$

$$\varepsilon_p(H)_{6061-\mathrm{O}} = 4.4836\left(H\right)^{6.3161} - 0.08 \ , \tag{16}$$

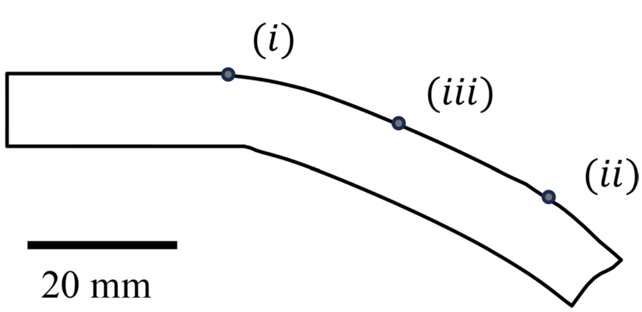

Fig. 3 Scaled cross-section of the preform showing the locations of tracked points used in the convergence study: (*i*) clamped region, (*ii*) roller contact area, and (*iii*) far-field free surface

where H is the measured Vickers hardness, ε_p is the equivalent plastic strain, and A, B, and ε_{ind} are empirically determined fitting parameters.

Results and discussion

The predictive capability of the finite element framework described above is examined through a twofold approach: numerical verification, ensuring stability and convergence of the simulations, and experimental validation, benchmarking the model against independent measurements of loads, geometry, temperature, and strain. Together, these studies establish both the reliability and physical accuracy of the computational methodology.

Verification

To ensure the accuracy and reliability of the numerical framework, a set of verification studies is done prior to validation against experimental measurements. Five simulations with progressively refined discretization, characterized by average tetrahedral element edge lengths of L equal to 1.55, 1.0, 0.8, 0.6,and 0.4 mm, are performed over the first 500 time steps. The 1.0, 0.6, and 0.4 mm meshes are used for Richardson extrapolation and calculation of the grid convergence index (GCI), providing an estimation of the order of convergence and mesh accuracy. The refinement ratio is taken as $r = \frac{0.6}{0.4} = 1.5$, the smaller of the two reductions.

On a global scale, discretization quality is assessed by monitoring volume drift, which in large deformation simulations is a key indicator of discretization error accumulation due to poor meshing or remeshing artifacts. After accounting for thermal expansion and elastic strain effects, the mesh plastic volume is found to increase by only 0.04% during the convergence studies, confirming good element quality and stable discretization.

For the five mesh sizes, three surface points near features of interest – (*i*) the clamped region, (*ii*) the roller contact, and (*iii*) the far-field free surface – are tracked, and the mechanical responses over time are collected over the 500 simulated time steps. Figure 3 shows the locations of these points relative to the preform cross-section.

Using the far-field point location (*iii*), the evolution of von Mises stress over time is plotted in Fig. 4, demonstrating that the stress response converges toward a common curve with increasing mesh refinement and decreasing average element edge length L across the five mesh sizes.

The localized plastic deformation induced by the rollers contributes the majority of work hardening and strain

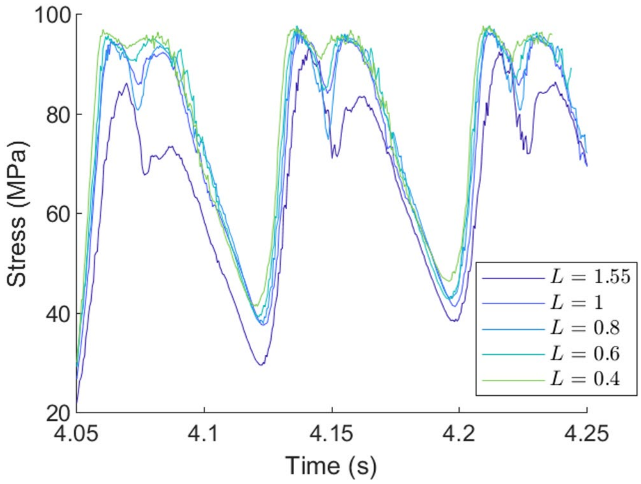

Fig. 4 Stress evolution at a representative point (*iii*) within the far-field region of the spin-formed preform, predicted in simulations performed with five different element edge length (L, in mm), demonstrating convergence of the stress response with decreasing L

accumulation in the preform, making convergence beneath the roller contact region critical. Using the tracked points underneath the roller (*ii*), the key properties of interest are recorded for each of the five mesh sizes. The properties of interest, including the discretized contact area between the roller and preform, von Mises stress, equivalent plastic strain, strain rate, temperature, and damage, are plotted against the reciprocal of element edge length $(1/L)$ in Fig. 5. Damage is defined as a non-dimensional parameter that relates strain and stress history to an estimate of the likelihood of tensile failure according to the Cockroft–Latham criterion [43]. Except for contact area, all properties are directly determined from the numerical implementation of the MTS constitutive model described above.

From the results shown in Fig. 5, contact area, von Mises stress, equivalent plastic strain, temperature, and damage all converge toward horizontal asymptotes with increasing mesh refinement, i.e., decreasing average element edge length. The strain rate, however, exhibits a slower convergence, with no clear asymptotic behavior observed within the explored range of edge lengths.

To further investigate the strain rate convergence, the maximum strain rates in the roller contact region are plotted in Fig. 6 for the five mesh sizes on a semi-log scale. A fitted logarithmic function (R^2 = 0.993) demonstrates that the strain rate increases approximately logarithmically with decreasing element length [40]. This agreement with an empirical logarithmic trend suggests that the strain rate exhibits a weak divergence, following an $O(log(1/L))$ rate, indicative of a localized singularity.

The possibility of discretization-induced singularities in contact stress problems has been discussed by Nayak, who investigated the emergence of weak singularities when relating elastic displacement to pressure within a contact region [44]. Similarly, Sinclair et al. highlighted convergence

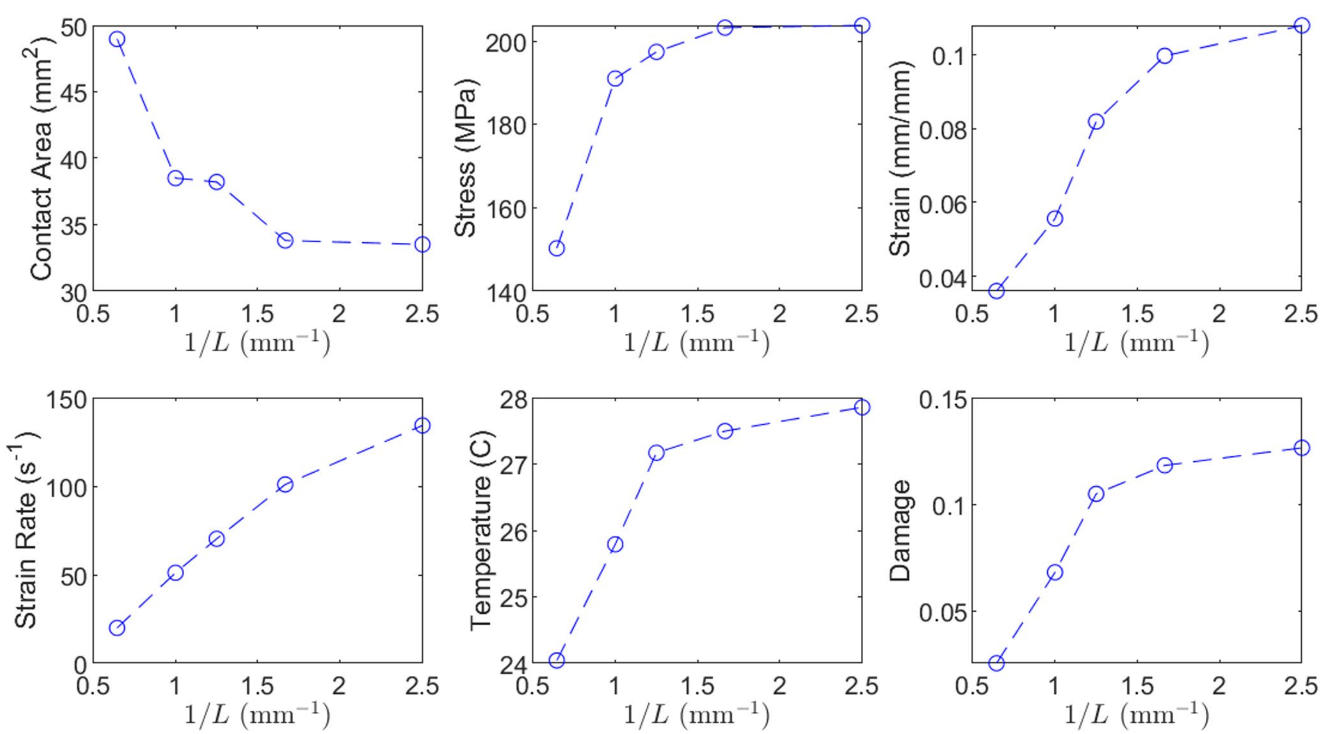

Fig. 5 Convergence of mechanical responses under the roller contact at point (*ii*). As the average edge length decreases ($1/L$ increases), most properties computed with the MTS constitutive model approach asymptotic values, while the strain rate exhibits slower convergence with increasing mesh refinement

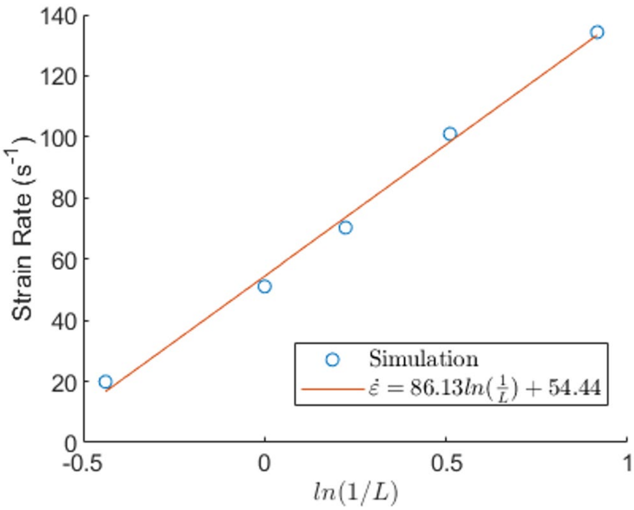

Fig. 6 Strain rate convergence under roller contact, showing that maximum strain rate scales logarithmically with element edge length. The logarithmic trend indicates slow divergence of strain rate with increasing mesh refinement

limitations in non-Hertzian contact [40], showing that numerical treatments of contact between mechanical tooling and the deforming body (modeled as instantaneous adjustment of nodal positions to conform to the contacting geometry) can generate a weak singularity at contact boundaries. At the onset of contact, time-sensitive variables such as strain rate may diverge indefinitely.

In contrast, the results from tracked point (*i*) in the clamped region, shown in Fig. 7, indicate that strain rates outside the immediate contact zone converge well, confirming that the selected mesh resolution is sufficient to capture large-deformation behavior away from contact singularities.

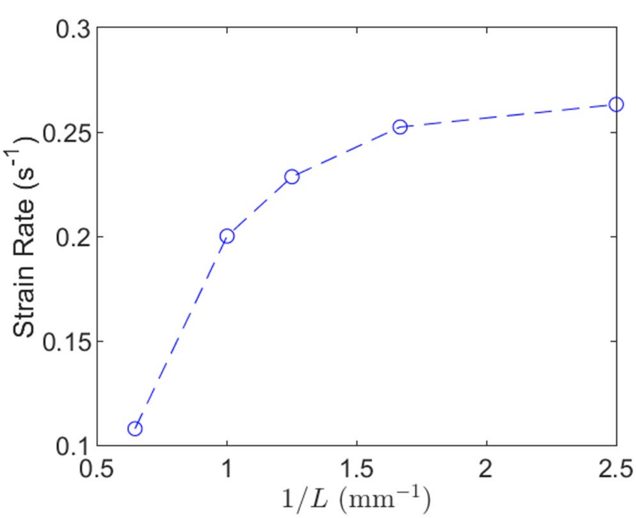

Fig. 7 Strain rate in the clamped region of the preform (point (*i*) in Fig. 3) as a function of mesh size, demonstrating convergence away from the roller contact and confirming global strain rate convergence in the preform

As a strategy to mitigate the contact singularity, strain rate in the roller contact region can be estimated through post-processing of the FEM strain results. Specifically, a continuous smoothed function is fitted to the accumulated strain, and the instantaneous strain rate is obtained as the time derivative of this fitted curve. This approach improves robustness by filtering out local oscillations and numerical noise present in the raw instantaneous strain rate output from the FEM. Figure 8 compares three strain-rate estimates at the far-field tracking point for a mesh size of $L = 0.6$ mm: (i) the raw FEM strain rate, (ii) the post-processed strain rate obtained as direct time derivative of strain, and (iii) the strain rate obtained as time derivative of the smoothed fitted strain. As shown in Fig. 8, application of the smoothed post-processing method eliminates the divergence associated with the contact singularity and enables consistent evaluation of strain-rate trends under the roller across different mesh sizes (Fig. 9).

In Fig. 9, the maximum strain rate under the roller exhibits the same qualitative convergence behavior as the von Mises stress in Fig. 5 and is considered convergent as a function of $1/L$. While the strain rates shown in Fig. 9 require post-processing, this approach provides a robust method for bounding the contact singularity and analytically estimating the strain rates imparted by the roller on the preform. The relative percent errors for the different mesh sizes compared to the theoretical value $f_{h=0}$ (as described by Eq. 13) are listed in Table 3. Three strain-rate measures are presented: instantaneous strain rate under the roller, instantaneous strain rate in the clamped region (no contact), and post-processed smoothed strain

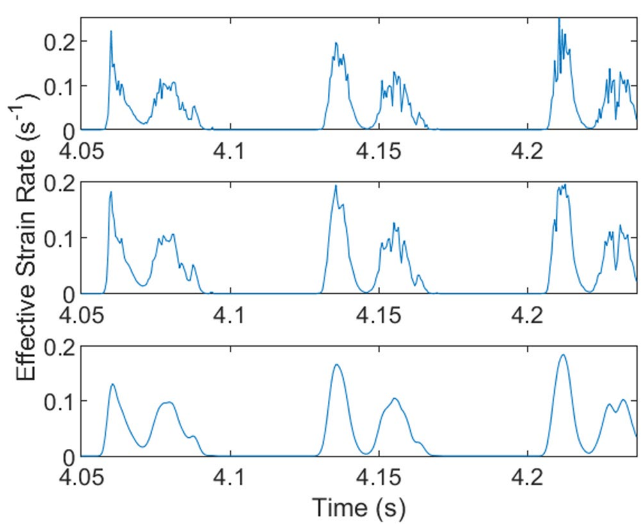

Fig. 8 Effect of strain-rate post-processing. Comparison of (top) raw FEM strain rate, (middle) time derivative of strain, and (bottom) time derivative of smoothed strain, showing the equivalence between instantaneous strain rate and the derivative-based approaches, with reduced noise after smoothing

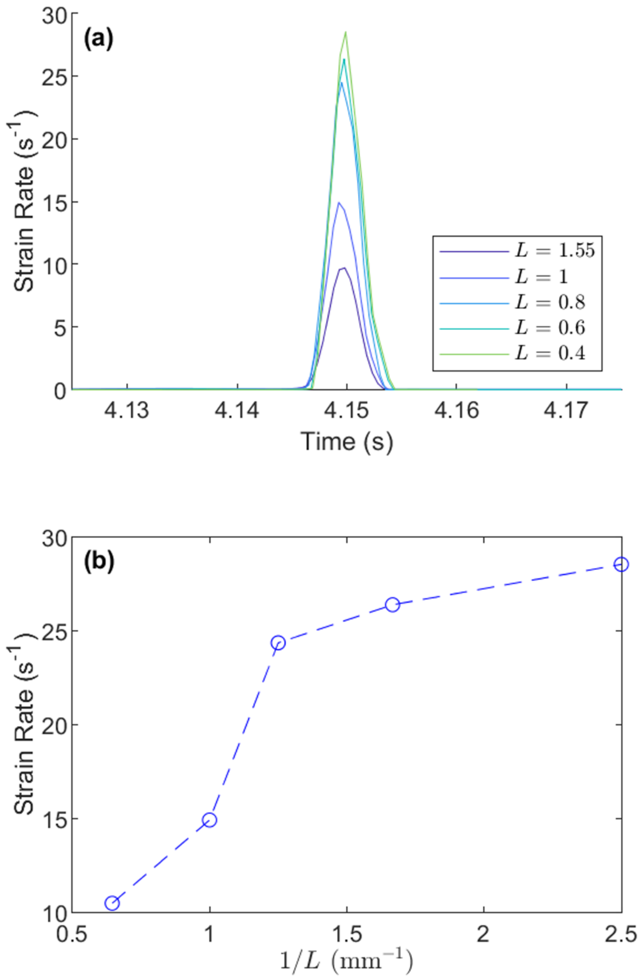

Fig. 9 Smoothed strain rate under the roller contact region, obtained as the time derivative of smoothed strain: (**a**) evolution over time and (**b**) maximum values as a function of element edge length. The results show that while instantaneous strain rate does not converge, the smoothed strain rate exhibits a consistent convergence with mesh refinement

rate from the roller contact region. These measures collectively illustrate convergence trends and quantify discretization error associated with the simulation outputs. Based on the results summarized in Table 3, a mesh size of 0.6 mm was selected for the refined region as the optimal balance between error reduction and computational efficiency, with discretization errors ranging from 0.3% to 9.2%.

Experimental validation

Following numerical verification, the model was validated against experimental measurements using four independent metrics: comparison of simulated and experimental roller loads, geometric cross-section tolerances, temperature evolution, and plastic strain distribution mapping.

Load comparisons

Reactionary tooling loads provide one of the most robust metrics for assessing deformation of thick preforms and the fidelity of the material constitutive model. In contrast to thin-walled forming, where variations in plastic response may be masked by lower force magnitudes, the force response of a thick, cantilevered preform accentuates material behavior, particularly in the post-yield plastic regime.

Four experimental loads were extracted from VUD-600 hydraulic data for a single five-pass spin-forming trial: vertical and radial loads for each of the two rollers. Experimentally, despite identical programming, the two rollers experience different loads due to minor positional variations and assembly tolerances, with up to 7 kN measured difference in loading. Despite these differences, the variations are repeatable, and individual rollers were found to be reproducible within ± 1.0 kN across nominally identical forming trials.

In the simulation, both rollers are modeled as positionally identical; therefore, only the loads from one simulated roller are presented and analyzed in Fig. 10. Both experimental and simulated load signals are smoothed using a moving average across 0.25% of the full dataset. Shaded regions in Fig. 10 indicate time intervals during which the rollers move downward or upward in the vertical direction, as illustrated by the toolpath shown in Fig. 1b.

From the finite element analysis, roller forces are computed from nodal surface stresses normal to the roller

Table 3 Discretization error for key results as a function of mesh size L, demonstrating convergence and decreasing error with mesh refinement. A 0.6 mm edge length was selected for the full-scale simulation as an optimal balance between accuracy and computational efficiency

L (mm)	1.55	1	0.8	0.6	0.4	GCI
Contact Area	46.3%	15.0%	14.1%	0.9%	0.1%	−0.0690%
Max Stress	−26.3%	−6.3%	−3.1%	−0.3%	0.0%	−0.0217%
Max Strain	−67.0%	−49.2%	−25.4%	−9.2%	−1.7%	−2.04%
Strain Rate	−90.1%	−74.6%	−65.1%	−49.8%	−33.3%	−26.1%
Strain Rate (no contact)	−59.3%	−24.7%	−14.1%	−5.1%	−1.1%	−0.789%
Strain Rate (smoothed)	−63.8%	−48.6%	−12.6%	−9.1%	−1.7%	−2.00%
Temperature	−14.0%	−7.7%	−2.8%	−1.6%	−0.3%	−0.204%
Damage	−80.1%	−46.9%	−18.1%	−7.7%	−1.3%	−1.57%

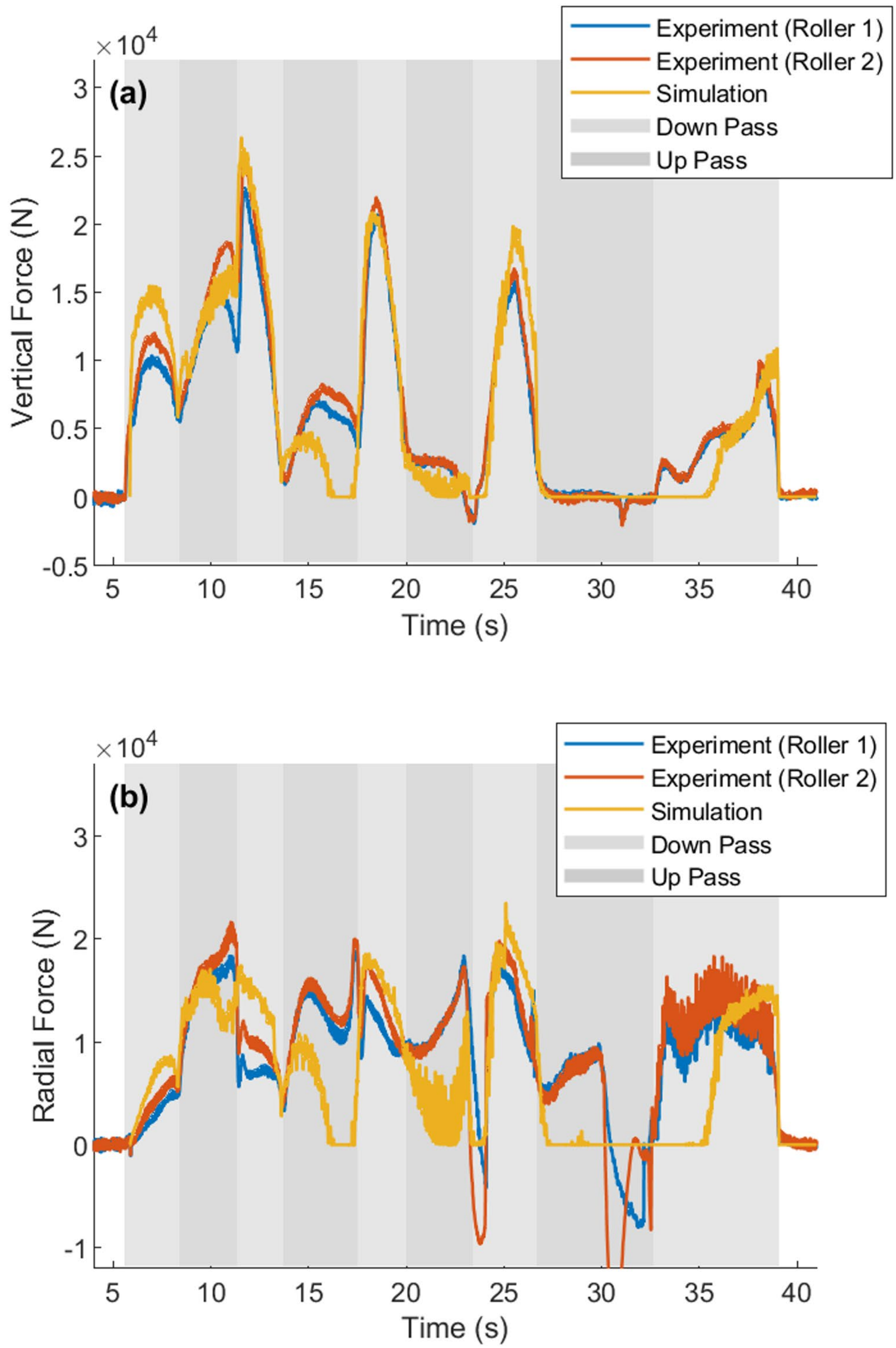

Fig. 10 Roller loads over time: (**a**) vertical and (**b**) radial components. The simulated loads (yellow) show good agreement with the experimentally measured roller forces in both peak magnitudes and temporal locations, particularly during the down-pass stages associated with large geometric deformation (light gray)

contact area. Good agreement with experimental measurements indicates that the MTS constitutive model accurately captures the global material flow stress response, particularly in the plastic regime near saturation stress and under varying temperature and strain rates.

Qualitatively, simulated forces show good agreement with the two experimental curves. Forces are slightly overpredicted during Down Pass 1 (Time < 8.4 s), likely due to minor positional variations in initial experimental contact relative to the simulation. These variations are most pronounced in Pass 1, which relies on absolute positioning of the roller and the preform. In subsequent passes, material deformation and plastic response are evaluated relative to the deformed geometry produced by the first pass.

After Down Pass 1, the simulated forces closely follow the experimentally measured forces in the subsequent Down Pass regions (light gray in Fig. 10). These Down Pass regions are where the majority of the bulk plastic work occurs, cantilevering the flat disk into its final cylindrical shape. Apart from Up Pass 1 (8.4 s < time < 11.3 s), the Up Pass regions (dark gray in Fig. 10; tool path shown in Fig. 1b) represent the time intervals when the rollers return to the clamped region and are designed to only skim the upper surface of the part rather than induce bulk deformation. The skimming generates a narrow bow wave of material, which is pushed toward the clamped zone. Experimental measurements indicate a bow wave height of approximately 1.2 mm, which is below the resolution threshold of the baseline mesh (1.55 mm edge length) outside the refined region. While finer mesh discretization could resolve this localized feature, such refinement would substantially increase computational cost without meaningfully improving the primary validation metrics of interest, namely through-thickness strain distributions and bulk cross-sectional geometry.

The force data observed in the Up Pass regions in Fig. 10 reflect the loss of this localized surface feature and suggest a slight underprediction of elastic springback. Inspection of the simulation data shows a resulting temporary loss of roller contact as the roller reapproaches the clamped region, most notably during Up Pass 4 (26.71 s < time < 32.68 s). Despite these localized discrepancies, the good agreement observed in the Down Pass deformation regions demonstrates that the model robustly captures the overall mechanical response during the forming process.

The local Down Pass maxima in vertical tooling loads, occurring near 6.8, 11.6, 18.5, 25.5, and 38.44 s, are the primary quantities of interest for load predictions. These peak forces provide practical bounds for assessing processability on the VUD-600 system and serve as indicators of the robustness of the material response model at extreme forming conditions. The values of the measured and calculated peak loads, along with corresponding percent differences between experimental and simulated results, are summarized in Table 4.

From Table 4, the largest variations occur in the lower-magnitude peaks, where experimental variability (±1.0 kN) is proportionally greater. Nevertheless, the simulation exhibits an average difference of 11–18% relative to experiment, which is comparable to the 15% difference observed between the two experimental rollers.

Geometric cross-sections

The geometric cross-sections of the preform measured in the experiment and predicted in the simulation are compared to assess dimensional accuracy of the modeling. Experimental cross-sections are generated by flattening 1° wedges of light-scanned point cloud data into a 2D cross-section from a one-pass preform, allowing evaluation of experimental tolerances and scanning precision. The VUD-600 forming machine is positionally controlled to within 10 µm tolerance, and the structured light scans have a resolution of 50 µm. Within these experimental limits, no significant deviations are observed between wedges of cross-sectional geometry. The simulated cross-section is extracted from the outer boundary in the middle of the refined 15° region. In addition to determining if the mesh size is appropriate for capturing features of interest, the geometric comparison also enables an evaluation of the elastic response, since the preform undergoes springback and slight geometric changes after the completion of spin forming. For Pass 1, the maximum simulated elastic springback was 0.3 mm in the vertical direction.

The deviations between experiment and simulation after Pass 1 (7.2 s), including springback, are illustrated in Fig. 11. The maximum deviation of 0.6 mm occurs at the outer edges of the preform, where the simulation assumes idealized right angles, while the experimental preform exhibits rounding from preparation steps, such as burr removal and edge finishing. Excluding these edge effects, the geometric deviation remains below 0.3 mm, demonstrating good agreement between simulation and experiment, particularly since the deviation is smaller than the mesh edge length (0.6 mm).

Table 4 Maximum vertical forming loads measured in the experiment and predicted in the simulation. Percent differences, Δ, are evaluated for the two rollers in the experiment (first row) and between the computational predictions and each of the two experimental rollers (two bottom rows)

		Down Pass 1	Down Pass 2	Down Pass 3	Down Pass 4	Down Pass 5	Average Difference
Roller 1 (Experiment)	Force	9.4 kN	22.0 kN	20.6 kN	17.2 kN	10.5 kN	
	Δ, %	25.4%	19.4%	10.4%	7.03%	11.76%	14.79%
Roller 2 (Experiment)	Force	12.6 kN	27.3 kN	23.0 kN	18.6 kN	11.9 kN	
		---	---	---	---	---	
Simulation to Roller 1 (Exp)	Force	15.4 kN	25.3 kN	20.8 kN	19.2 kN	10.5 kN	
	Δ, %	63.8%	15.0%	0.97%	11.6%	0.0%	18.27%
Simulation to Roller 2 (Exp)	Force	---	---	---	---	---	
	Δ, %	22.2%	7.33%	9.57%	3.78%	11.76%	10.92%

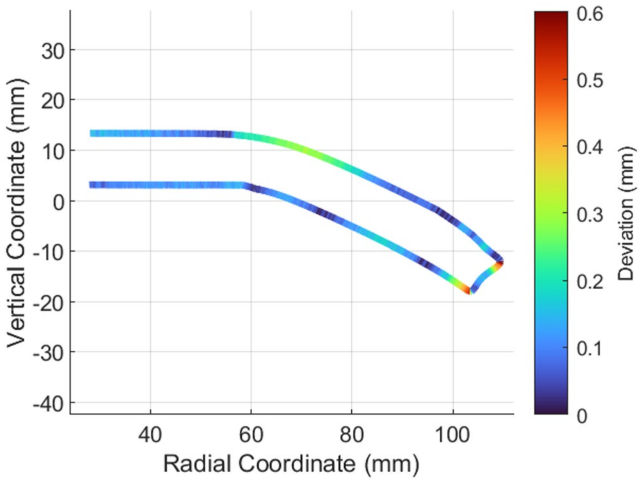

Fig. 11 Simulated geometric cross section, colored to show deviation from experimental cross section of the preform after Pass 1 (7.2 s). The results demonstrate that the predicted geometry matches experiment within 0.3 mm, except at edge regions affected by preparation rounding. The deviation is smaller than the refined mesh resolution (0.6 mm), confirming adequate spatial accuracy of the simulation.

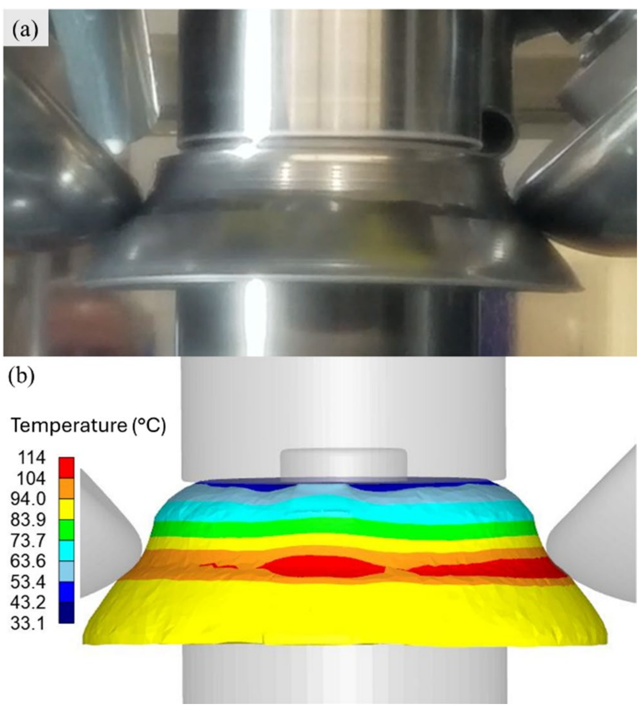

Fig. 12 Semi-quantitative validation of temperature accumulation: (**a**) video still showing the first observation of steam formation at a time of 17.1 s, indicating that local temperature exceeds 100 °C, and (**b**) simulated temperature distribution at the corresponding time, highlighting the thermal gradient in the roller–preform contact region

Temperature accumulation

Temperature validation is performed at a semi-quantitative level. Direct temperature measurement is challenging due to the rotary motion of the preform, which limits thermocouple placement. Moreover, severe plastic deformation, evolving curvature, and the low emissivity and high reflectivity of aluminum precludes reliable use of conventional infrared thermography. As a result, thermal validation is done at a semi-quantitative level, through visual observations during forming (Fig. 12).

Steam formation is first observed around 17 s into the process (Pass 3), implying that the preform temperature locally exceeds 100 °C. The simulation predicts a similar trend, with the roller–preform contact region surpassing 100 °C within the same time frame and remaining above this threshold thereafter. This agreement provides confidence that the heat generation model, which assumes conversion of mechanical work into heat, captures the magnitude and timing of thermal accumulation during the forming process.

Hardness strain mapping

Beyond global validation using tooling loads, accumulated strain provides a means to assess work hardening distributions and evaluate the model's ability to capture through-thickness deformation in the spin-formed part.

For validation, the clamped and roller contact regions, where strain accumulation is highest, are selected for analysis in a representative preform after Pass 1. The experimental strain distribution is obtained by smoothing Vickers indentation hardness maps (1×1 mm square spacing, 308 indentations in the clamped region and 204 in the roller contact region) and converting the values to plastic strain using Eq. 16. Of note, the indentations cannot be performed on a sample edge, so the experimental plots show the inner distribution approximately 1.5 mm away from the preform edges. Dotted lines in Figs. 13 and 14 are used to show the boundary edges of the experimental cross-sections. In the simulation, the equivalent plastic von Mises strain is plotted for direct comparison.

Although individual indentation measurements may be influenced by local microstructural features such as precipitates or grain boundaries, the 100-gf indentation load prescribed by ASTM E384 [28] ensures bulk material response. Moreover, the spatial density of measurements enables construction of a global strain field that is robust against isolated outliers, facilitating meaningful comparison with the simulated strain distributions.

As shown in Figs. 13 and 14, both the spatial distribution and magnitudes of strain exhibit good agreement between simulation and experiment. In the clamped region, Fig. 13, the effective plastic strain predicted along the top surface is 0.219 mm/mm, compared to 0.208 mm/mm from indentation measurements. Considering the experimental confidence band (±0.02 mm/mm at low strain, increasing to ±0.15 mm/mm for strains of ~2), the experimental and

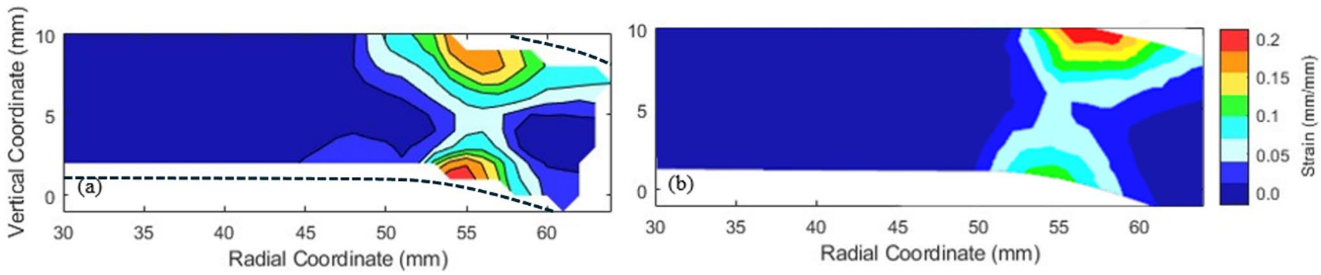

Fig. 13 Experimental (**a**) and simulated (**b**) effective plastic strain distributions in the clamped region (*i*) after Pass 1, showing good agreement between the measured and predicted strain fields

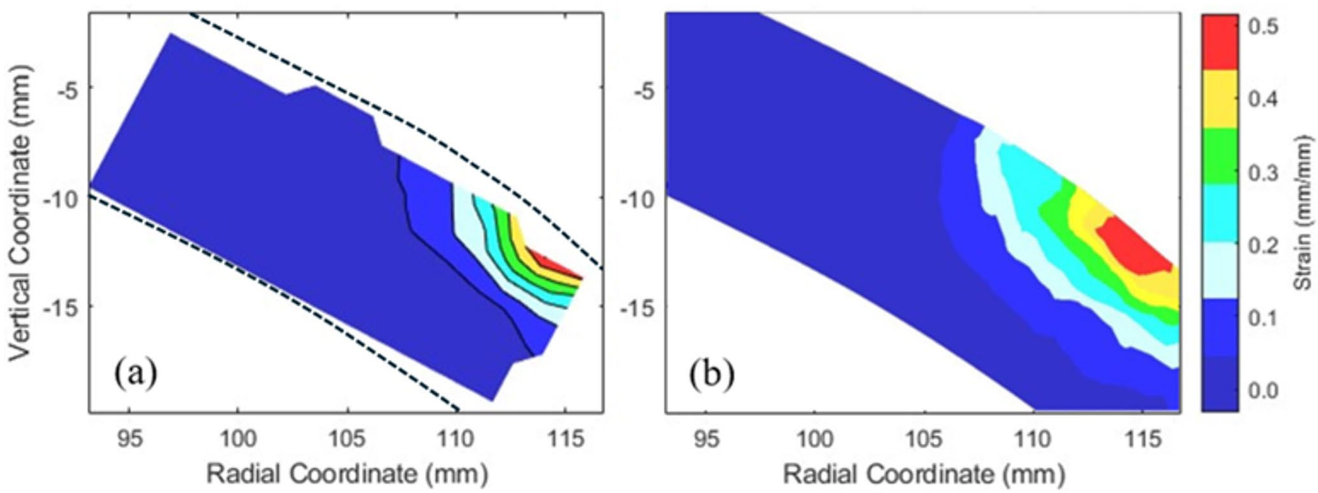

Fig. 14 Experimental (**a**) and simulated (**b**) effective plastic strain distributions in the roller contact region after Pass 1, showing good agreement in the magnitude and distribution of plastic strain between measurement and simulation

simulated results fall within mutual uncertainty ranges. Similarly, in the vicinity of roller contact, Fig. 14 shows consistent strain distributions across the cross-section, with maximum values of 0.439 mm/mm (experiment) and 0.495 mm/mm (simulation), again confirming good agreement between predicted and measured strain fields.

Figures 13 and 14 further highlight the pronounced through-thickness variation in accumulated effective plastic strain, underscoring the importance of developing a fully resolved 3D finite element model. Even after completion of forming and subsequent elastic springback, the preform retains effective plastic strains exceeding 0.4 mm/mm beneath the localized roller contact region (Fig. 14). The retained plastic strain leads to locally heterogeneous mechanical response, in stark contrast to the mid-thickness and inner surface regions, which accumulate negligible plastic strain (≈0.0 mm/mm) during the first spin forming pass. As spin forming continues to be adopted as an advanced manufacturing process, quantitative understanding of the spatial distribution of accumulated strain, and its implications for final mechanical properties, is essential for informed process optimization and reliable part quality prediction.

Conclusions

This study establishes an experimentally validated finite element modeling framework for spin forming of Al 6061-O, demonstrating robust predictive capabilities for through-thickness deformation in spin-formed parts.

The main findings are as follows:

1. The *Mechanical Threshold Stress (MTS) constitutive law* accurately captures both the elastic and plastic responses of Al 6061-O over the range of strain rates and temperatures relevant to spin forming, with path dependence captured through the evolution of effective strain magnitude.
2. The computational model is shown to be *numerically converged and verified*. A refined 15° wedge with an average element edge length of 0.6 mm provides an effective balance between accuracy in material response and computational efficiency.
3. *Multi-modal experimental validation*, including roller forces, deformation geometry, temperature evolution, and plastic strain distributions, confirms the predictive

accuracy of the model. The consistency across four independent validation methods provides strong confidence in the ability of the MTS constitutive law to globally describe the material response.

4. The model predicts *average peak roller loads within 11–18% of experiment*, *geometric tolerances within 3%*, and *plastic strain distributions within 10%*, all of which fall within the uncertainty bounds of the experimental data.
5. Despite the demonstrated accuracy of the model, *computational cost remains a significant limitation*: a full spin-forming simulation takes nearly a month of runtime on a desktop workstation. This motivates future efforts focused on reduced-order modeling strategies and optimization of meshing, convergence, and solver schemes. Nevertheless, the framework presented in this paper provides a robust and quantitatively validated benchmark against which future simplified and reduced-order approaches can be evaluated.

Overall, this work provides a *validated and transferable modeling framework* for spin forming that can be extended to other metallic material systems, supporting predictive process design and enabling improved understanding of the complex deformation mechanisms governing spin-formed components.

Acknowledgements Special thanks are given to the Computational Materials Group at the University of Virginia and the Advanced Materials and Processing Branch at NASA Langley Research Center. In particular, the authors would like to thank and credit Cecilia Mulvaney and Harold Claytor of NASA Langley for their experimental support conducting spin forming experiments and hardness measurements. The authors would like to thank the NASA Advanced Air Transport Technology (AATT) project and the Virginia Space Grant Consortium (VSGC) for the support of this work.

Author contributions E.U. and L.Z. wrote the main manuscript text and E.U. prepared all figures. All authors reviewed the manuscript.

Funding This study was funded by the NASA Advanced Air Transport Technology (AATT) project and the Virginia Space Grant Consortium (VSGC).

Data availability The data that support the findings of this study are not openly available due to reasons of sensitivity and are available from the corresponding author, Elizabeth Urig, upon reasonable request. Data are located in controlled access data storage at NASA Langley Research Center.

Declarations

Competing interests The authors declare no competing interests.

References

1. Bylya OI, Ward M, Krishnamurty B, Tamang S, Vasin RA (2017) Modelling challenges for incremental bulk processes despite advances in simulation technology: example issues and approaches. Procedia Eng 207:2358–2363. https://doi.org/10.1016/j.proeng.2017.10.1008
2. Bylya OI, Khismatullin T, Blackwell P, Vasin RA (2018) The effect of elasto-plastic properties of materials on their formability by flow forming. J Mater Process Technol 252:34–44. https://doi.org/10.1016/j.jmatprotec.2017.09.007
3. Music O, Allwood JM, Kawai K (2010) A review of the mechanics of metal spinning. J Mater Process Technol 210:3–23. https://doi.org/10.1016/j.jmatprotec.2009.08.021
4. Sariyarlioglu EC, Music O, Bakkal M (2022) Backward tube spinning mechanics. Int J Adv Manuf Technol 123:479–491. https://doi.org/10.1007/s00170-022-10100-x
5. Follansbee PS (2014) On the definition of state variables for an internal state variable constitutive model describing metal deformation. Mater. Sci. Appl. 5:603–609. https://doi.org/10.4236/msa.2014.58062
6. Roula AM, Mocellin K, Traphöner H, Tekkaya AE, Bouchard PO (2022) Influence of mechanical characterization on the prediction of necking issues during sheet flow forming process. J Mater Process Technol 306:117620. https://doi.org/10.1016/j.jmatprotec.2022.117620
7. Perić D, Owen DRJ (2017) Computational modeling of forming processes. Encyclopedia of computational mechanics, 2nd ed. Wiley, New York, pp 1–51. https://doi.org/10.1002/9781119176817.ecm2037
8. Biba N, Vlasov A, Stebunov S, Maximov A (2015) An approach to simulation of flow forming using elastic-visco-plastic material model. In: *13th International cold forming congress*, Glasgow, pp 141–147
9. Li R, Zheng Z, Zhan M, Zhang H, Lei Y (2021) Fracture prediction in spin forming of anisotropic metal sheets. Proceedings of the Institution of Mechanical Engineers, Part C: Journal of Mechanical Engineering Science 235:7743–7758. https://doi.org/10.1177/09544062211042044
10. Jawale K, Loukaides EG (2019) An investigation of mandrel-free spinning. Procedia Manuf 29:145–152. https://doi.org/10.1016/j.promfg.2019.02.119
11. Russo I, Cleaver C, Allwood J, Loukaides E (2020) The influence of part asymmetry on the achievable forming height in multi-pass spinning. J Mater Process Technol 275:116350. https://doi.org/10.1016/j.jmatprotec.2019.116350
12. Sebastiani G, Brosius A, Homberg W, Kleiner M (2007) Process characterization of sheet metal spinning by means of finite elements. Key Eng Mater 344:637–644. https://doi.org/10.4028/www.scientific.net/KEM.344.637
13. Rentsch B, Manopulo N, Hora P (2017) Numerical modelling, validation and analysis of multi-pass sheet metal spinning

processes. Int J Mater Form 10:641–651. https://doi.org/10.1007/s12289-016-1308-5
14. Mohebbi MS, Akbarzadeh A (2010) Experimental study and FEM analysis of redundant strains in flow forming of tubes. J Mater Process Technol 210:389–395. https://doi.org/10.1016/j.jmatprotec.2009.09.028
15. Krishnamurthy B, Shitikov AA, Blackwell P, Bylya O (2023) Influence of mesh in modelling of flow forming process. Materials Research Proceedings 28:1583–1592. https://doi.org/10.21741/9781644902479-171
16. Zhang P, Zhao CH, Wu TF, Han JC (2025) Forming mechanism and regulation of microstructural evolution for stainless steel tube with annular inner ribs by the method of hot power spinning. Int J Mater Form 18:54. https://doi.org/10.1007/s12289-025-01916-5
17. Jiang S, Zheng Y, Ren Z, Li C (2009) Multi-pass spinning of thin-walled tubular part with longitudinal inner ribs. Trans Nonferrous Met Soc China 19:215–221. https://doi.org/10.1016/S1003-6326(08)60255-1
18. Cao TS (2017) Models for ductile damage and fracture prediction in cold bulk metal forming processes: a review. Int J Mater Form 10:139–171. https://doi.org/10.1007/s12289-015-1262-7
19. Bouhamed A, Jrad H, Said LB, Wali M, Dammak F (2019) A non-associated anisotropic plasticity model with mixed isotropic–kinematic hardening for finite element simulation of incremental sheet metal forming process. Int J Adv Manuf Technol 100:929–940. https://doi.org/10.1007/s00170-018-2782-3
20. Bishnoi P, Chandna P (2022) Formability of aluminum alloys during single point incremental forming: a review. Int J Manuf Mater Mech Eng 12:1–26. https://doi.org/10.4018/IJMMME.296277
21. Follansbee PS (2014) Fundamentals of strength: Principles, experiment, and applications of an internal state variable constitutive formulation. Springer, Cham, Switzerland. https://doi.org/10.1007/978-3-031-04556-1
22. Kuykendall KL (2011) *An evaluation of constitutive laws and their ability to predict flow stress over large variations in temperature, strain, and strain rate characteristic of friction stir welding*. Dissertation, Brigham Young University. https://scholarsarchive.byu.edu/etd/2768
23. Boddorff A, Mulvaney C, Tayon W (2024) Influence of feedrate on microstructure and hardness of conventionally spin-formed 6061-O plate. In: Wagstaff, S. (ed) *Light Metals 2024*. TMS 2024. The Minerals, Metals & Materials Series. Springer, Cham, Switzerland. https://doi.org/10.1007/978-3-031-50308-5_18
24. Stegall D, Hales S, Tayon W, Mulvaney C, Urig E, Boddorff A, Taminger K (2024) Advances in integrally formed metallic structures. 2nd Annual Worldwide Advanced Manufacturing Symposium for Space, Air and Land Transportation, Orlando, FL
25. Urig E, Zhigilei L (2023) Finite element modeling of plastic deformation during spin forming of aluminum 6061-O. Virginia Space Grant Consortium (VSGC) 2023 Student Research Conference, Newport News, VA. https://vsgc.odu.edu/wp-content/uploads/2023/05/Urig_Paper.pdf Accessed 14 October 2025
26. Urig E, Zhigilei L (2024) Implementation of internal state variable constitutive model for finite element analysis of rotary forming processes. Virginia Space Grant Consortium (VSGC) 2024 Student Research Conference, Newport News, VA https://vsgc.odu.edu/wp-content/uploads/2024/04/Urig_VSGC_Paper__Final.pdf Accessed 14 October 2025
27. Varshni YP (1970) Temperature dependence of the elastic constants. Phys Rev B 2:3952–3958. https://doi.org/10.1103/PhysRevB.2.3952
28. Mecking H, Nicklas B, Zarubova N, Kocks UF (1986) A universal temperature scale for plastic flow. Acta Metall 34:527–535. https://doi.org/10.1016/0001-6160(86)90088-X
29. Kocks UF, Argon AS, Ashby MF (1975) *Thermodynamics and kinetics of slip*. Progress in materials science, vol 19. Pergamon, Oxford
30. Kocks UF, Mecking H (2003) Physics and phenomenology of strain hardening: the FCC case. Prog Mater Sci 48:171–273. https://doi.org/10.1016/S0079-6425(02)00003-8
31. DEFORM V12.1.1 Manual (2021) Scientific Forming Technologies Corporation, Columbus, OH
32. Mulvaney MC, Stegall DE, Hales SJ, Taminger KMB, FitzGerald JM, Agnew SR (2025) Utilizing strain rate jump testing to predict incremental spin formability of Al alloys sensitive to Portevin–Le Chatelier instabilities. Integrating Mater Manuf Innov 14:25–39. https://doi.org/10.1007/s40192-024-00379-x
33. ABAQUS Theory Manual (2025) (v6.6), Heat generation caused by plastic straining. https://classes.engineering.wustl.edu/2009/spring/mase5513/abaqus/docs/v6.6/books/stm/default.htm?startat=ch04s03ath112.html. Accessed 1 June 2025
34. Kobayashi S, Oh S-I, Altan T (1989) Metal forming and the finite-element method. Oxford University Press, New York
35. Hasselström AKJ, Nilsson U (2012) *Thermal contact conductance in bolted joints*. Dissertation, Chalmers University of Technology. https://hdl.handle.net/20.500.12380/159027
36. *Structural alloys handbook* Holt JM, Technical, Ho E CY, (eds) (1996) CINDAS/Purdue University, West Lafayette, IN
37. Savaş A, Pamuk MT, Seçgin Ö, Arda E (2020) Numerical modeling of friction stir welding using experimental temperature data. Emerg Mater Res 9:499–505. https://doi.org/10.1680/jemmr.18.00080
38. Roache PJ (2009) Fundamentals of verification and validation. Hermosa Publishers, Socorro, New Mexico
39. Slater J (2024) Examining spatial (grid) convergence, NPARC alliance CFD verification and validation. https://www.grc.nasa.gov/www/wind/valid/tutorial/spatconv.html Accessed 25 October
40. Sinclair GB, Beisheim JR, Sezer S Practical convergence-divergence checks for stresses from FEA. Proc. 12th Int. ANSYS Conf. 2006, Pittsburgh, Pennsylvania (2006) https://cdm.ing.unimore.it/dokuwiki/_media/wikipaom2016/sinclair_et_al_practical_convergence_divergenze_checks_for_stresses_from_fea.pdf Accessed 14 October 2025
41. Urig E, Stegall D (2025) Hardness-strain correlation for rolled Al 6061-O plate validated by finite element modeling. NTRS - NASA Technical Reports Server, NASA Langley Research Center
42. Haghshenas M, Wood JT, Klassen RJ (2012) Investigation of strain-hardening rate on splined mandrel flow forming of 5052 and 6061 aluminum alloys. Mater Sci Eng A 532:287–294. https://doi.org/10.1016/j.msea.2011.10.094
43. Cockcroft MG, Latham DJ (1968) Ductility and the workability of metals. J Inst Met 96:33–39
44. Nayak L (1982) Singularity consideration in numerical solution of contact stress problems. J Lubr Technol 104:352–356. https://doi.org/10.1115/1.3253218

Publisher's note Springer Nature remains neutral with regard to jurisdictional claims in published maps and institutional affiliations.